

## Article

# Nonlinear Finite Element Analysis and Fatigue Damage Assessment of Wind-Induced Vibration for the Tension Cable-Supported Power Transmission Structure

Jingyang Li <sup>1</sup>, Bangjie Wang <sup>1</sup>, Tao Wang <sup>2,3,\*</sup> and Zhengliang Li <sup>1,4</sup>

<sup>1</sup> School of Civil Engineering, Chongqing University, Chongqing 400045, China; jingyanglic@163.com (J.L.); bangjiewang@cqu.edu.cn (B.W.); lizhengl@hotmail.com (Z.L.)

<sup>2</sup> School of Transportation Science and Engineering, Harbin Institute of Technology, Harbin 150090, China

<sup>3</sup> Chongqing Research Institute of Harbin Institute of Technology, Harbin Institute of Technology, Chongqing 401151, China

<sup>4</sup> Chongqing Key Laboratory of Wind Engineering and Wind Resources Utilization, Chongqing 400045, China

\* Correspondence: taowang@alu.cqu.edu.cn

**Abstract:** The tension cable-supported power transmission structure (TC-PTS) is a new type of power transmission structure suitable for mountainous terrain, and is sensitive to wind load. In this regard, a nonlinear finite element analysis model of wind-induced vibration is proposed for the TC-PTS, and the wind-induced vibration response of the structure is analyzed. Firstly, the tangent stiffness matrix of the three-dimensional truss element for the supporting suspension cable and transmission line, considering the geometric nonlinearity of structures, is derived through the relationship between the element elastic energy and its displacement. Subsequently, the element mass matrix and damping matrix of the supporting suspension cable and transmission line, as well as the element nodal load vector obtained from wind load equivalence, are given. Then, based on the nonlinear finite element theory, the nonlinear dynamic equation of wind-induced vibration is established for the TC-PTS and solved using the Newmark- $\beta$  method combined with the Newton-Raphson iterative method. Furthermore, the rain-flow counting method and Miner's linear fatigue cumulative damage theory were used for wind-induced fatigue damage assessment. Finally, a two-span TC-PTS was selected as an example, and the wind-induced nonlinear vibration and fatigue damage assessment were analyzed through the proposed model. The results show that the proposed model has high computational accuracy and efficiency. The first three order vibration modes of the supporting-conductor part of the two-span TC-PTS were antisymmetric vertical bending, symmetric side bending, and antisymmetric side bending. With the increase in wind speed and wind direction angle, the maximum lateral displacement and tension of the supporting suspension cable and transmission line increased, and their degree of increase showed a nonlinear trend. In terms of the wind-induced fatigue analysis results of TC-PTS, the fatigue damage at the end of the supporting-conductor suspension cable was greater than the fatigue damage at its midpoint. Compared to the fatigue damage at the midpoint of the conductor, the fatigue damage at the end of the conductor was less affected by the wind direction angle, and both were more significantly affected by the wind speed.

**Keywords:** tension cable-supported power transmission structure; wind-induced vibration; nonlinear finite element; wind-induced fatigue damage



**Citation:** Li, J.; Wang, B.; Wang, T.; Li, Z. Nonlinear Finite Element Analysis and Fatigue Damage Assessment of Wind-Induced Vibration for the Tension Cable-Supported Power Transmission Structure. *Buildings* **2023**, *13*, 2924. <https://doi.org/10.3390/buildings13122924>

Academic Editor: Fabio Rizzo

Received: 22 September 2023

Revised: 5 November 2023

Accepted: 21 November 2023

Published: 23 November 2023



**Copyright:** © 2023 by the authors. Licensee MDPI, Basel, Switzerland. This article is an open access article distributed under the terms and conditions of the Creative Commons Attribution (CC BY) license (<https://creativecommons.org/licenses/by/4.0/>).

## 1. Introduction

As a part of electric energy infrastructure, a high-voltage transmission tower-line system is an important part of the transmission and distribution systems in the power grid [1]. With the boom in the development of power grid construction, the number of power transmission structures erected in mountainous terrains has been increasing [2]. However, the paths required for transmission line corridors in mountainous areas are

becoming tighter, and the selection of tower locations is becoming increasingly difficult. For example, in the karst terrain of Guangxi, the Danxia terrain of Xinjiang, and other special and complex mountainous terrain in China, tower positions of the transmission tower-line system are often difficult to set up, owing to terrain restrictions, resulting in a wide range of line rerouting.

Therefore, in recent years, the electric power industry has begun the investigation of new power transmission structures that are well-suited for mountainous areas. A typical structure is the tension cable-supported power transmission structure (TC-PTS), which is a new form of overhead power transmission structure. The TC-PTS primarily consists of a conductor, ground wire, supporting-conductor suspension cable, supporting-ground wire suspension cable, tension-resistant insulator strings, and fixed brackets. The structural schematics are illustrated in Figure 1. Among them, the supporting suspension cable made of high-strength steel strands is the main load-bearing structure, and is usually fixed in mountain rock or rigid fixed brackets, with the transmission line through the connection of fittings and the supporting suspension cable forming a coupling system.

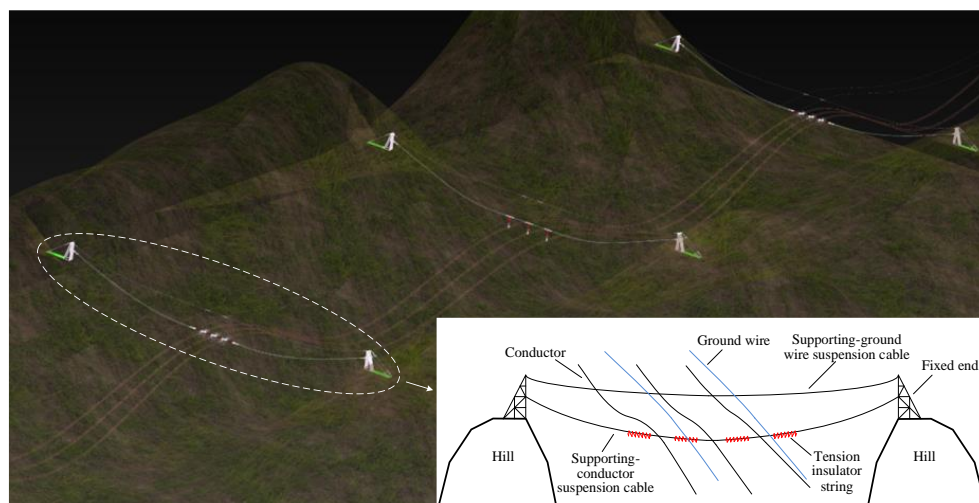


**Figure 1.** Schematic diagram of the tension cable-supported power transmission structure.

The supporting suspension cables and transmission lines in TC-PTS are large-span, highly flexible spatial suspension structures, and are typical wind-sensitive structures. In addition, the structures have mechanical characteristics such as large deformation and small strain, and the geometric nonlinear effect is significant. Compared with the transmission line and transmission tower-line systems, the transmission line of the TC-PTS forms a more flexible coupled system with supporting suspension cables, and its geometric nonlinear effect is more significant. Scholars have conducted a series of studies to address the wind-induced nonlinear vibration problem of transmission lines and transmission tower line systems. In early studies, transmission lines were usually considered to be suspension structures, and their static and dynamic characteristics were analyzed [3–5]. With the development of the finite element method and large deformation theory, the wind-induced vibration analysis of transmission lines and tower-line systems is generally performed using a nonlinear finite element method. The mechanical model of the transmission line and the tower-line system based on the truss element is convenient for performing various types of wind vibration and other static and dynamic analysis [6,7]. The mechanical model of the transmission line and tower-line system established using a cable element and beam element can consider the torsional and bending capacity of the transmission line and then study complex wind vibration problems such as galloping [8–13]. Scholars have examined the dynamic models of transmission lines and tower-line systems in depth, as well as the nonlinear vibration issues generated by wind, using rigorous theoretical investigations and numerical simulations. These studies have resulted in noteworthy study outcomes.

However, nonlinear dynamic modeling and wind-induced vibration analyses of TC-PTS have rarely been reported. In addition, TC-PTS is prone to wind-induced fatigue damage under the wind load, and it is necessary to evaluate the wind-induced fatigue of TC-PTS. The rain-flow method and the equivalent structural stress method [14,15] are often used for the wind-induced fatigue assessment. In order to evaluate the safety of TC-PTS, a framework for the wind-induced fatigue assessment needs to be proposed.

To this end, this study establishes a finite element model of TC-PTS based on 3D truss elements, then the nonlinear dynamic equations of the structure are formed, and the iterative solution process of the Newmark- $\beta$  method combined with the Newton-Raphson method is provided. In addition, wind vibration fatigue assessment was performed by combining the rainfall counting method with the Miner linear fatigue cumulative damage theory. The remainder of this paper is organized as follows: Section 2 exhibits the simplified mechanical model of TC-PTS. The nonlinear finite element equation of wind-induced vibration and fatigue damage assessment method for TC-PTS is shown in Section 3. Subsequently, Section 4 provides an example and the corresponding discussion. Finally, some conclusions are summarized in Section 5.

## 2. Simplified Mechanical Model of TC-PTS

### 2.1. Structural Parameters and Boundary Conditions

The simplified model and the structural parameters of the TC-PTS are shown in Figure 2.  $l_s$  is the horizontal distance between the ends on both sides of the same suspension cable,  $l_c$  is the horizontal distance between two adjacent spans of the suspension cable,  $h_s$  is the height difference between the ends of both sides of the same suspension cable,  $h_c$  is the height difference between the positions of the same span of the conductor or ground wire in the adjacent hanging points of the suspension cable, and  $h_{wg}$  is the height difference between the ends of the supporting-ground wire suspension cable and the corresponding ends of the supporting-conductor suspension cable.

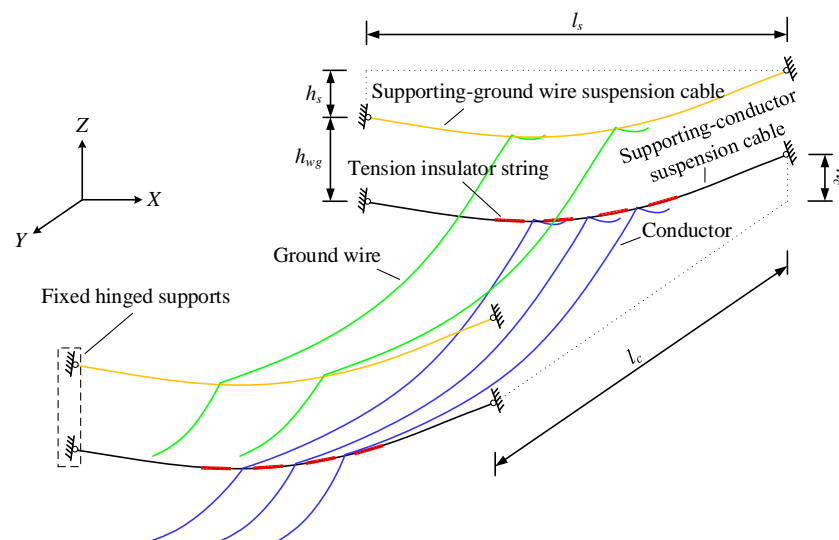


**Figure 2.** Simplified model and structural parameters of the tension cable-supported power transmission structure.

The connections between the ends of the supporting suspension cables, the fixed supports, and the connections between the transmission lines and corresponding suspension cables at the boundaries are hinged. Therefore, all the supports at the TC-PTS boundary can be considered as fixed hinged supports.

## 2.2. Initial Shape of TC-PTS

To establish a finite element model of the TC-PTS that considers the geometric non-linear effect, it is necessary to first obtain the initial shape and initial internal force under gravity loading. For the supporting suspension cables and transmission lines of the TC-PTS, the initial shape can be simplified as a parabolic model, and the functional expression required to establish this parabolic model is

$$y = 4xf_m(1 - x/l)/l \quad (1)$$

where  $y$  is the vertical distance from the calculation point to the starting point,  $x$  is the horizontal distance from the calculation point to the starting point,  $l$  is the horizontal distance from the end point to the starting point, and  $f_m$  is the spanning mid-arc droop calculated according to Equation (2):

$$f_m = ql^2 / (8\sigma_0 \cos \beta) \quad (2)$$

where  $q$  is the gravity load per element volume of the supporting suspension cable or transmission line,  $\sigma_0$  is the horizontal stress of the suspension cable,  $\beta$  is the angle of elevation difference, and  $\tan\beta = h/l$ , where  $h$  is  $h_s$  or  $h_c$  and  $l$  is the corresponding  $l_s$  or  $l_c$ .

## 2.3. The Mechanical Characteristics of TC-PTS

In TC-PTS, the supporting suspension cables and transmission lines are mainly subjected to tension, and to a lesser extent, they will also be subjected to bending and torsional moments. It is reasonable to neglect the bending and torsional capacities in wind vibration response analysis without considering torsion [16]. Therefore, in the TC-PTS wind vibration analysis, the supporting suspension cables and transmission lines were primarily considered for the axial tensile capacity.

## 3. Nonlinear Finite Element Analytical Model of Wind-Induced Vibration and Fatigue Damage Assessment for TC-PTS

### 3.1. Element Stiffness Matrix for Supporting Suspension Cables and Transmission Lines

According to the mechanical characteristics of the TC-PTS, its supporting suspension and transmission line wind vibration are large deformation and small strain problems. Combined with the force characteristics of this power transmission structure, the finite element model shown in Figure 3 can be established using a 3D truss element by considering geometric nonlinear effects. Generally, the element stiffness matrix can be established using both the local and global coordinate systems. Compared with the stiffness matrix established in the local coordinate system [13,17,18], the element stiffness matrix in the global coordinate system [19–21] can be directly grouped into the system stiffness matrix. It can be directly grouped into a system stiffness matrix to effectively avoid the coordinate conversion process. For the three-dimensional truss element in the global coordinate system, the stiffness matrices are mostly derived using the principle of virtual work [19] and by deriving the truss ends [21]. However, the virtual work principle requires multiple integrals, and often results in implicit stiffness matrices that are difficult to apply directly, whereas the truss end strives for derivatives that require more complicated vector operations. Therefore, this study simplifies the operation through the relationship between the elastic energy of the 3D truss element and its deformation, and derives the explicit stiffness matrix of the 3D truss element under the global coordinate system.

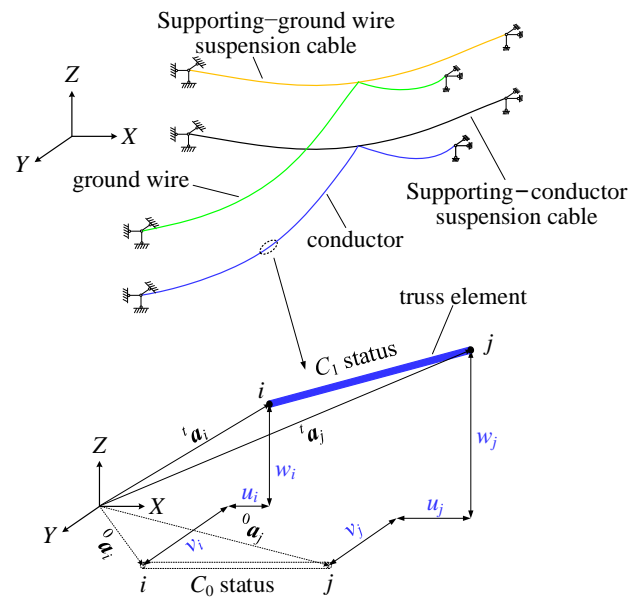


Figure 3. Simplified finite element model and node displacements.

In Figure 3, the physical quantities at the initial moment ( $C_0$  state) are known quantities, and the node vectors at both ends of the element in the global coordinate system are

$$\begin{cases} {}^0\mathbf{a}_i = \{ x_i & y_i & z_i \}^T \\ {}^0\mathbf{a}_j = \{ x_j & y_j & z_j \}^T \end{cases} \quad (3)$$

The principle of vector subtraction is then used to obtain the element vectors of the truss element in the global coordinate system.

$${}^0\mathbf{a}_e = {}^0\mathbf{a}_j - {}^0\mathbf{a}_i = \{ x_j - x_i \quad y_j - y_i \quad z_j - z_i \}^T \quad (4)$$

After time  $t$ , the truss element undergoes a displacement deformation movement to  $C_1$  state, and the displacement vector of the nodes at both ends of the element under the global coordinate system is

$$\begin{cases} \mathbf{u}_i = \{ u_i & v_i & w_i \}^T \\ \mathbf{u}_j = \{ u_j & v_j & w_j \}^T \end{cases} \quad (5)$$

From Equations (3) and (5), the node vectors at both ends of the element in the global coordinate system are

$$\begin{cases} {}^t\mathbf{a}_i = {}^0\mathbf{a}_i + \mathbf{u}_i \\ {}^t\mathbf{a}_j = {}^0\mathbf{a}_j + \mathbf{u}_j \end{cases} \quad (6)$$

Therefore, the element vector of the truss element at time  $t$  is

$${}^t\mathbf{a}_e = {}^0\mathbf{a}_e + \mathbf{u}_j - \mathbf{u}_i \quad (7)$$

According to the node displacement vector, the element displacement vector can be expressed as

$$\mathbf{u}_e = \{ u_i \quad v_i \quad w_i \quad u_j \quad v_j \quad w_j \}^T \quad (8)$$

Equation (7) can be further expressed as Equation (8) as

$${}^t\mathbf{a}_e = {}^0\mathbf{a}_e + [-\mathbf{I}_{3 \times 3} \quad \mathbf{I}_{3 \times 3}] \mathbf{u}_e \quad (9)$$

where  $\mathbf{I}_{3 \times 3}$  is the 3rd order element matrix.

At  $C_0$  state, the truss element in the state has no strain and its element length is

$${}^0l = |{}^0\mathbf{a}_e| = \sqrt{{}^0\mathbf{a}_e^T {}^0\mathbf{a}_e} \quad (10)$$

At  $C_1$  state, the length of the truss element in the state is

$${}^t l = |{}^t\mathbf{a}_e| = \sqrt{{}^t\mathbf{a}_e^T {}^t\mathbf{a}_e} \quad (11)$$

At this point, the strain in the truss element is

$${}^t\varepsilon = ({}^t l - {}^0l) / {}^0l \quad (12)$$

The truss element elastic energy  ${}^tU$  at time  $t$  can be calculated using Equation (13):

$${}^tU = \int_V \int_0^{{}^t\varepsilon} \sigma(\varepsilon) d\varepsilon dV \quad (13)$$

where  $\sigma(\varepsilon)$  is the stress of the truss element, and the relationship between stress and strain in the linear elastic range is  $\sigma(\varepsilon) = E\varepsilon$ ,  $E$  is the Young's modulus,  $V$  is the element volume, and when the cross-section area of the truss element is a constant value of  $A$ , Equation (13) can be further expressed as

$${}^tU = \frac{1}{2} EA {}^0l {}^t\varepsilon^2 \quad (14)$$

The element tangent stiffness matrix at time  $t$  in the global coordinate system can be calculated using the Hessian matrix, as follows:

$${}^t\mathbf{K}_e = \frac{\partial^2 {}^tU}{\partial {}^t\mathbf{u}_e \partial {}^t\mathbf{u}_e^T} \quad (15)$$

The final result of the element tangent stiffness matrix at time  $t$  is:

$${}^t\mathbf{K}_e = \frac{EA {}^t\varepsilon}{{}^t l} \begin{bmatrix} \mathbf{I}_{3 \times 3} & -\mathbf{I}_{3 \times 3} \\ -\mathbf{I}_{3 \times 3} & \mathbf{I}_{3 \times 3} \end{bmatrix} + \frac{EA}{{}^t l^3} \begin{bmatrix} {}^t\mathbf{a}_e {}^t\mathbf{a}_e^T & -{}^t\mathbf{a}_e {}^t\mathbf{a}_e^T \\ -{}^t\mathbf{a}_e {}^t\mathbf{a}_e^T & {}^t\mathbf{a}_e {}^t\mathbf{a}_e^T \end{bmatrix} \quad (16)$$

The element tangent stiffness matrix  ${}^t\mathbf{K}_e$  shown in Equation (16) is derived by introducing only the linear elasticity assumption and not the small deformation assumption, which is an exact tangent stiffness matrix at any displacement. Therefore, it is applicable to the case of arbitrarily large deformations and small strains.

### 3.2. Element Mass Matrix and Damping Matrix

The TC-PTS finite element model mass matrix is constructed using a consistent mass matrix with an element-consistent mass matrix, as follows:

$$\mathbf{M}_e = \frac{{}^0l \rho A}{6} \begin{bmatrix} 2\mathbf{I}_{3 \times 3} & \mathbf{I}_{3 \times 3} \\ \mathbf{I}_{3 \times 3} & 2\mathbf{I}_{3 \times 3} \end{bmatrix} \quad (17)$$

where  ${}^0l$  is the initial length of the element and  $\rho$  is the mass density of the element, respectively.

The element damping matrix is constructed using Rayleigh damping:

$${}^t\mathbf{C}_e = \alpha_v \mathbf{M}_e + \beta_v {}^t\mathbf{K}_e \quad (18)$$

where  $\alpha_v$  and  $\beta_v$  are the Rayleigh damping constants calculated using Equations (19) and (20):

$$\alpha_v = 2\xi_{k1} \omega_{k1} \omega_{k2} / (\omega_{k1} + \omega_{k2}) \quad (19)$$

$$\beta_v = 2(\xi_{k2}\omega_{k2} - \xi_{k1}\omega_{k1})/(\omega_{k1}^2 + \omega_{k2}^2) \quad (20)$$

where  $\omega_{k1}$  and  $\omega_{k2}$  are the intrinsic frequencies of the  $k1$ st and  $k2$ nd order modes, respectively;  $\xi_{k1}$  and  $\xi_{k2}$  are the damping ratios corresponding to the  $k1$ st and  $k2$ nd order modes, respectively. This can be considered as  $\beta_v = 0$  [22]. In this case,  ${}^tC_e$  is not affected by the change in structural displacement, namely,  $C_e$ .

### 3.3. Equivalent Nodal Load Vector

The primary loads to which the TC-PTS was subjected were gravity and wind. The static and dynamic displacements of this power transmission structure are based on the gravity load equilibrium position. Therefore, when calculating the structural equivalent nodal load vector, the gravity load is equivalent to the internal nodal load vector at the reference position. For the truss elements of the TC-PTS finite element model, the wind load per unit length was calculated using Equation (21):

$$F_D = \frac{1}{2}\rho_{air}V_z^2C_D A_m \quad (21)$$

where  $\rho_{air}$  is the air density,  $V_z$  is the wind speed,  $C_D$  is the drag coefficient, and  $A_m$  is the windward projected area per unit length of the truss element, for supporting suspension cables  $A_m = d\cos\theta$ , for transmission lines  $A_m = d\sin\theta$ ,  $d$  is the diameter of the truss element, and  $\theta$  is the angle of the wind direction (shown in Figure 4).

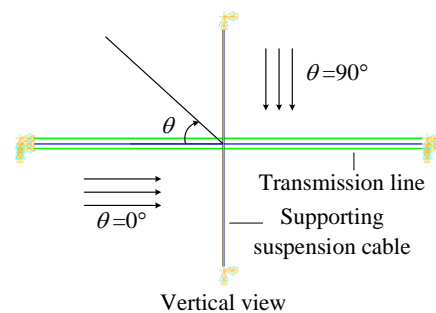


**Figure 4.** Schematic diagram of wind direction angle  $\theta$ .

$V_z$  can be calculated using Equation (22):

$$V_z = V_s(z) + V(t) \quad (22)$$

where  $V_s(z)$  is the average wind speed and  $V(t)$  is the pulsating wind speed.

The pulsating wind speed  $V(t)$  is generated by the harmonic synthesis method [23]. The average wind speed  $V_s(z)$  can be calculated from the exponential law according to Equation (23):

$$V_s(z) = (z/10)^\alpha V_{10} \quad (23)$$

where  $V_{10}$  is the reference average wind speed at the height of 10 m,  $z$  is the height, and  $\alpha$  is the ground roughness coefficient. As TC-PTS is in the mountainous terrain, its ground roughness category can be considered as C. According to the “Code for Structural Loads of Buildings” [24],  $\alpha$  is taken as 0.22.

The wind loads on the element are converted to element equivalent nodal loads, namely:

$${}^tF_e = \frac{1}{2}{}^t l [F_{ix} \ F_{iy} \ F_{iz} \ F_{jx} \ F_{jy} \ F_{jz}]^T \quad (24)$$

where  $F_{ix}$  is the equivalent nodal load of the wind load in the  $X$ -direction at node  $i$ , and the rest are similar.

### 3.4. Establishment of the Nonlinear Dynamic Equation

The mass matrix, stiffness matrix, damping matrix, and equivalent nodal load vectors of each element of the TC-PTS were assembled, respectively, and the nonlinear dynamic equations of the structure were established based on the updated Lagrangian formulation at the reference position:

$$\mathbf{M}^{t+\Delta t}\ddot{\mathbf{u}} + \mathbf{C}^{t+\Delta t}\dot{\mathbf{u}} + {}^{t+\Delta t}\mathbf{Q} - {}^0\mathbf{Q} = {}^{t+\Delta t}\mathbf{F} \quad (25)$$

where  ${}^{t+\Delta t}\ddot{\mathbf{u}}$  and  ${}^{t+\Delta t}\dot{\mathbf{u}}$  are the acceleration and velocity vectors of the structure at time  $t+\Delta t$ , and  $\mathbf{M}$  and  $\mathbf{C}$  are the mass and damping matrix of the structure.  ${}^{t+\Delta t}\mathbf{Q}$  and  ${}^0\mathbf{Q}$  are the internal load vectors; that is, the internal nodal load vectors at time  $t + \Delta t$  and the reference position, respectively. In addition,  ${}^{t+\Delta t}\mathbf{F}$  is the equivalent nodal load vector of the structure at time  $t + \Delta t$ .

When  $\Delta t$  is sufficiently small, the displacement increment of the structure within a time step is small, and  ${}^{t+\Delta t}\mathbf{Q}$  and  ${}^t\mathbf{K}$  can be approximated using the following linear relationship:

$${}^{t+\Delta t}\mathbf{Q} = {}^t\mathbf{Q} + {}^t\mathbf{K}\mathbf{u} \quad (26)$$

where  ${}^t\mathbf{Q}$  is the internal nodal load vector at time  $t$ ,  ${}^t\mathbf{K}$  is the stiffness matrix of the structure at time  $t$ , and  $\mathbf{u}$  is the displacement increment within  $\Delta t$ ; that is  $\mathbf{u} = {}^{t+\Delta t}\mathbf{u} - {}^t\mathbf{u}$ .

Combining Equations (25) and (26), the nonlinear dynamic equation in the form of displacement increments can be obtained:

$$\mathbf{M}^{t+\Delta t}\ddot{\mathbf{u}} + \mathbf{C}^{t+\Delta t}\dot{\mathbf{u}} + {}^t\mathbf{K}\mathbf{u} = {}^{t+\Delta t}\mathbf{F} - [{}^t\mathbf{Q} - {}^0\mathbf{Q}] \quad (27)$$

### 3.5. Solution of the Nonlinear Dynamical Equation

The Newmark- $\beta$  method is used to solve the nonlinear finite element equations shown in Equation (27). Because Equation (26) is a linear approximation, the displacement increment of the solution produces a large error accumulation as the time step increases. Therefore, to improve the accuracy of the solution and avoid the accumulation of numerical instability within each time step, the Newton-Raphson iterative method was used in this study for balanced iterative calculation. The solution process is summarized as follows.

Step 1: Calculate the individual element characterization matrices  ${}^0\mathbf{K}_e$ ,  $\mathbf{M}_e$ , and  $\mathbf{C}_e$  based on the initial shape and strain of the element, and then assemble them to obtain the characterization matrices  ${}^0\mathbf{K}$ ,  $\mathbf{M}$ , and  $\mathbf{C}$  of the structure.

Step 2: Apply the initial equivalent nodal load  ${}^0\mathbf{F}$ , and then calculate  ${}^0\ddot{\mathbf{u}}$  from the initial conditions  ${}^0\mathbf{u}$  and  ${}^0\dot{\mathbf{u}}$ :

$${}^0\ddot{\mathbf{u}} = \mathbf{M}^{-1}[{}^0\mathbf{F} - \mathbf{C}{}^0\dot{\mathbf{u}} - {}^0\mathbf{K}{}^0\mathbf{u}]$$

Step 3: Select the time step  $\Delta t$  and calculate the integration constant [25] using the known physical quantities at time  $t$ . The effective stiffness matrix was calculated before performing the iterations of  ${}^t\hat{\mathbf{K}}^{(0)}$ :

$${}^t\hat{\mathbf{K}}^{(0)} = {}^t\mathbf{K} + c_0\mathbf{M} + c_1\mathbf{C}$$

Step 4: Perform Newton-Raphson iterations. Calculate the effective load vector  ${}^{t+\Delta t}\hat{\mathbf{F}}$  at time  $t + \Delta t$ :

$${}^{t+\Delta t}\hat{\mathbf{F}} = {}^{t+\Delta t}\mathbf{F} + \mathbf{M}[c_0{}^t\mathbf{u} + c_2{}^t\dot{\mathbf{u}} + c_3{}^t\ddot{\mathbf{u}}] + \mathbf{C}[c_1{}^t\mathbf{u} + c_4{}^t\dot{\mathbf{u}} + c_5{}^t\ddot{\mathbf{u}}]$$

From this, calculate the unbalanced force vector for the first iteration  ${}^{t+\Delta t}\hat{\mathbf{F}}^{(0)}$ :

$${}^{t+\Delta t}\hat{\mathbf{F}}^{(0)} = {}^{t+\Delta t}\hat{\mathbf{F}} - [{}^t\mathbf{Q}^{(0)} - {}^0\mathbf{Q}] - [c_0\mathbf{M} + c_1\mathbf{C}][{}^{t+\Delta t}\mathbf{u}^{(0)} - {}^t\mathbf{u}]$$

where  ${}^t\mathbf{Q}^{(0)}$  is the internal nodal load vector before the first iteration, and  ${}^{t+\Delta t}\mathbf{u}^{(0)}$  is the displacement before the first iteration, namely  ${}^t\mathbf{u}$ .

Solve for the displacement increment  $\mathbf{u}^{(1)}$  after the first iteration at time  $t + \Delta t$ :

$$\mathbf{u}^{(1)} = [{}^t\hat{\mathbf{K}}^{(0)}]^{-1} [{}^{t+\Delta t}\hat{\mathbf{F}}^{(0)}]$$

Step 5: Update  ${}^t\mathbf{K}^{(1)}$  and  ${}^t\mathbf{Q}^{(1)}$  and update the effective stiffness matrix  ${}^t\hat{\mathbf{K}}^{(1)}$  and the displacement before iteration  ${}^{t+\Delta t}\mathbf{u}^{(1)}$ :

$${}^{t+\Delta t}\mathbf{u}^{(1)} = {}^{t+\Delta t}\mathbf{u}^{(0)} + \mathbf{u}^{(1)}$$

and the unbalanced force vector  ${}^{t+\Delta t}\hat{\mathbf{F}}^{(1)}$ :

$${}^{t+\Delta t}\hat{\mathbf{F}}^{(1)} = {}^{t+\Delta t}\hat{\mathbf{F}} - [{}^t\mathbf{Q}^{(1)} - {}^0\mathbf{Q}] - [c_0\mathbf{M} + c_1\mathbf{C}][{}^{t+\Delta t}\mathbf{u}^{(1)} - {}^t\mathbf{u}]$$

and calculate the displacement increment after the second iteration  $\mathbf{u}^{(2)}$ :

$$\mathbf{u}^{(2)} = [{}^t\hat{\mathbf{K}}^{(1)}]^{-1} [{}^{t+\Delta t}\hat{\mathbf{F}}^{(1)}]$$

Step 6: Determine whether the L2 norm of the unbalanced force vector  ${}^{t+\Delta t}\hat{\mathbf{F}}^{(1)}$  satisfies the convergence condition; if not, loop Step 5 until the convergence condition is satisfied; if so, end the Newton–Raphson iteration to obtain the final nonlinear displacement  ${}^{t+\Delta t}\mathbf{u}$  at time  $t+\Delta t$ , and then obtain the velocity  ${}^{t+\Delta t}\dot{\mathbf{u}}$  and acceleration  ${}^{t+\Delta t}\ddot{\mathbf{u}}$  at time  $t + \Delta t$ .

### 3.6. Wind-Induced Fatigue Damage Assessment of TC-PTS

Using the displacement time history and velocity time history obtained from the above TC-PTS wind vibration nonlinear finite element analysis model, the stress time history of each part of the TC-PTS could be derived. The rain-flow counting method was then used to process the stress time history and obtain the stress amplitude distribution statistically. Finally, the number of stress cycles in which fatigue damage occurs can be obtained using the  $S$ – $N$  curve. The logarithmic form of the  $S$ – $N$  curve is shown in Equation (28):

$$\lg N = C - m \lg S \quad (28)$$

where  $N$  is the number of stress cycles in which fatigue damage occurs,  $C$  and  $m$  are the material fatigue parameters, and  $S$  is the stress amplitude.

The fatigue parameters for support suspension materials [26] were obtained from  $C = 13.84$  and  $m = 3.5$ . The fatigue parameters of the transmission line materials [27] are available for  $N \leq 2 \times 10^7$ ,  $C = 13.27$ , and  $m = 5$ , as well as for  $N > 2 \times 10^7$ ,  $C = 14.40$ , and  $m = 5.95$ .

According to Miner's linear fatigue cumulative damage criterion, the wind vibration fatigue damage of each part of the TC-PTS is as follows:

$$D = \sum_{i=1}^k n_i / N_i \quad (29)$$

where  $D$  is the total fatigue damage value. When  $D = 1$ , fatigue damage occurs,  $k$  is the total number of stress amplitudes,  $n_i$  is the number of times the  $i$ th stress amplitude occurs, and  $N_i$  is the number of stress cycles corresponding to the  $i$ th stress amplitude where fatigue damage occurs.

In addition, wind vibration fatigue damage analysis of the supported suspension cables and transmission lines must consider the effect of the average stress. The Goodman model is often used to correct for the effect of the nonzero average stress  $S_m$ , namely:

$$S = S_0(1 - S_m/S_t) \quad (30)$$

where  $S$  is the actual stress amplitude,  $S_0$  is the equivalent stress amplitude at zero average stress,  $S_m$  is the average stress, and  $S_t$  is the tensile strength of a material.

#### 4. Example Analysis

##### 4.1. Example Description

In this study, a two-span TC-PTS, as shown in Figure 5, was considered as the research object for wind vibration response analysis and fatigue damage assessment. The Kaimal spectrum was used as the wind speed power spectral density function, the wind speed time duration was taken as 600 s, the structural parameters of the two-span TC-PTS were  $l_s = 1000$  m,  $l_c = 800$  m,  $h_{wg} = 20$  m,  $h_s = 0$  m, and  $h_c = 0$  m, respectively, and the endpoints of the supporting-conductor suspension cables were considered to be fixed at a height of 300 m. All the calculations required for the analysis in this study were performed on a computer with an Intel i5-9400F CPU (manufactured by Intel, Santa Clara, CA, USA) and 32 GB of RAM (manufactured by Corsair Memory, Fremont, CA, USA).

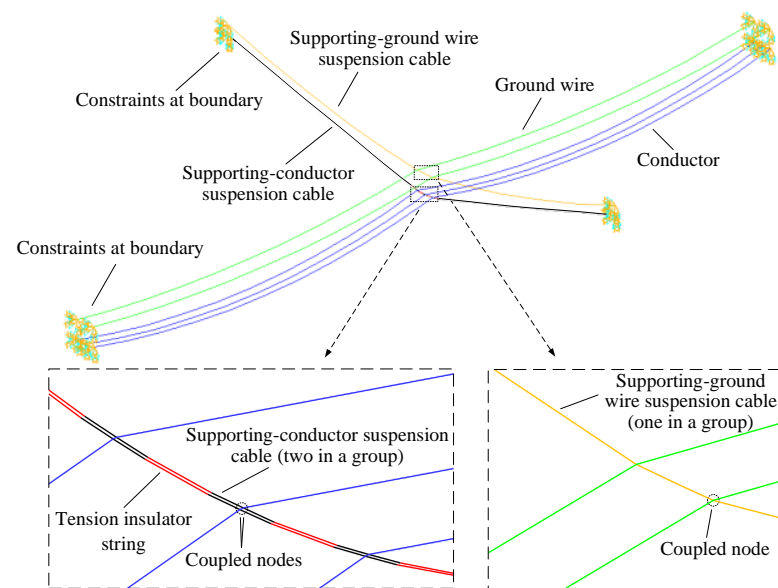


**Figure 5.** A two-span tension cable-supported power transmission structure.

Using the proposed model, the first five orders of natural frequency and the first three orders of the vibration mode of this power transmission structure can be calculated, as shown in Table 1 and Figure 6, respectively. The results of the frequency analysis in Table 1 show that the first five orders of intrinsic frequencies of the supporting-conductor part are 77.89%, 78.65%, 78.28%, 78.30%, and 78.30% of the corresponding values of the supporting-ground wire part. The lower-order natural frequency of the supporting-conductor part was lower than that of the supporting-ground wire part. As shown in Figure 6, for the supporting-conductor part, the first-, second-, and third-order vibration modes were anti-symmetric vertical bending, symmetric lateral bending, and antisymmetric lateral bending, respectively.

**Table 1.** First five orders of natural frequency of TC-PTS.

Parts	Frequency Order	Proposed Model/(Hz)	ANSYS/(Hz)
The supporting-conductor part	first order	0.08063	0.08063
	second order	0.08174	0.08174
	third order	0.08186	0.08186
	fourth order	0.08188	0.08188
	fifth order	0.08188	0.08188
The supporting-ground wire part	first order	0.1035	0.1035
	second order	0.1039	0.1039
	third order	0.1046	0.1046
	fourth order	0.1046	0.1046
	fifth order	0.1046	0.1046

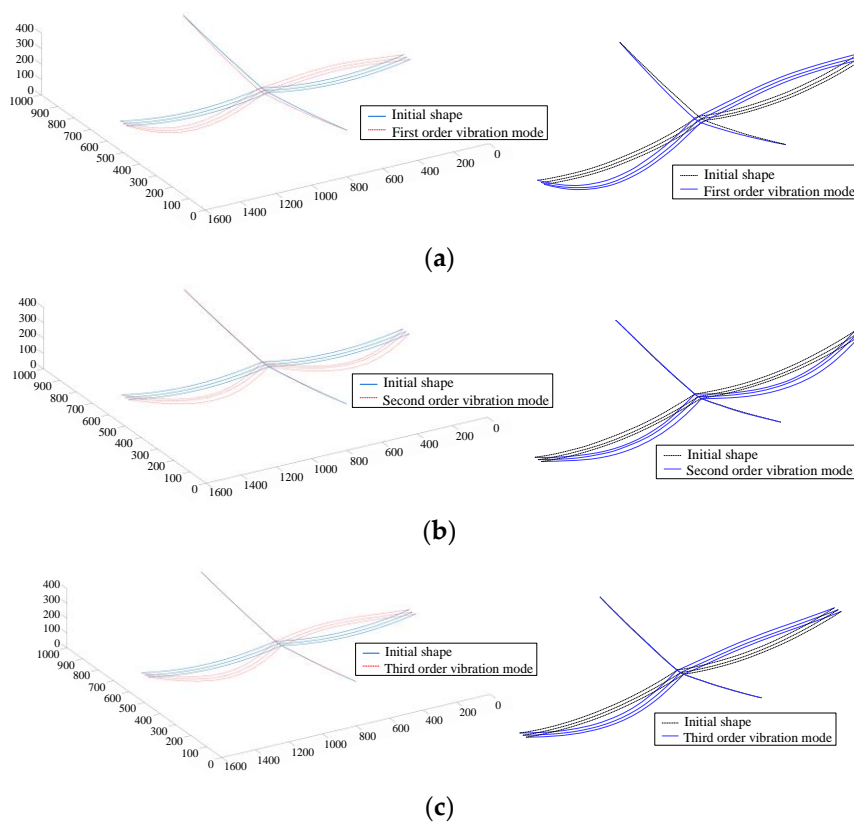


**Figure 6.** First three orders mode of vibration of the supporting-conductor part obtained by the proposed model (left) and ANSYS (right). (a) First order vibration mode; (b) second order vibration mode; (c) third order vibration mode.

To verify the correctness and calculation accuracy of the proposed model, ANSYS (ANSYS, Inc., Canonsburg, PA, USA) was used to perform a modal analysis, and the results of the two calculations were compared. In the ANSYS model, the supporting suspension and transmission lines were simulated using the Link180 element, and the structural parameters, boundary conditions, and other parameters were consistent with those of the model in this study. The ANSYS calculation results are also given in Table 1 and Figure 6, respectively, and it can be seen that the maximum absolute value of the relative error of the frequency results of the proposed model is 0.001%, which is more accurate, and the vibration modes are also consistent.

## 4.2. Wind-Induced Vibration Response of TC-PTS

### 4.2.1. Time History Analysis of TC-PTS Wind-Induced Vibration Response

The time history analysis of the wind-induced vibration response of TC-PTS was performed by considering the working conditions of the wind speed  $V_{10} = 15\text{m/s}$  and wind direction angle  $\theta = 90^\circ$ . The standard deviation ( $\sigma$ ) of the lateral displacement time history results at each node position of a single span conductor in TC-PTS is shown in Figure 7, and it can be seen that the standard deviation of lateral displacement in the center of the conductor is the largest, which is 2.34 m, indicating that the location in the center of the conductor is more significantly affected by wind load, and the standard deviation values of lateral displacement in the remaining locations are roughly symmetrical along the location in the center of the conductor. The lateral displacement time histories at the center of the conductor are shown in Figure 8, and the average and maximum values of the lateral displacement time histories in Figure 8 are listed in Table 2. The results in Table 2 and Figure 8 show that the average value of lateral displacement in the conductor under wind load in this condition is 23.33 m, and its maximum value is 29.70 m. The lateral displacement is distributed from the minimum value of 16 m to the maximum value of 29.70 m, with a large variation.

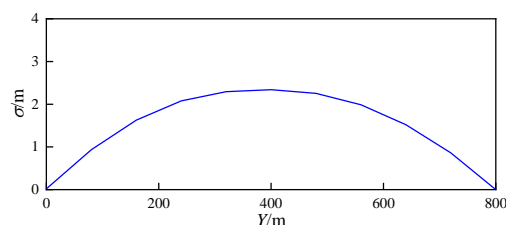


**Figure 7.** Mean square deviation of lateral displacement at each position of a single-span conductor.

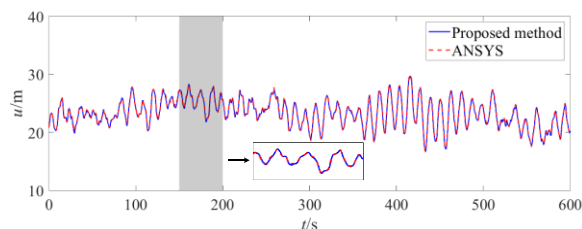


**Figure 8.** The lateral displacement time history of the conductor midpoint.

**Table 2.** Average and maximum values obtained by the proposed model and ANSYS.

Terms	Average Values	Maximum Values
Proposed model	23.33m	29.70 m
ANSYS	23.36m	29.95 m
Relative error/(%)	0.13	0.83

Similarly, the time history of the midpoint displacement of the conductor computed by ANSYS is plotted in Figure 8 and Table 2, whereas the computational efficiency of the proposed model is listed in Table 3. From Figure 8 and Table 2, it can be observed that the relative errors of the mean and maximum values of the lateral displacement time history obtained by the proposed model were 0.13% and 0.83%, respectively, and its accuracy was high. Simultaneously, the lateral displacement time history curves obtained by the proposed model had a consistent trend with the ANSYS results, which had a high degree of agreement. The results in Table 3 show that the computation time required by ANSYS to analyze the lateral displacement in the conductor was 35.88 min, whereas the computation time of the proposed model was 1.50 min, and its computational cost was only 4.19% of

the former. Therefore, the proposed model can be applied to the wind-induced vibration nonlinear finite element analysis for TC-PTS more efficiently.

**Table 3.** Calculation efficiency obtained by the proposed model and ANSYS.

Terms	Computing Time/min	Calculation Efficiency/%
Proposed model	1.50	4.19
ANSYS	35.88	-

#### 4.2.2. Effect of Different Wind Direction Angles on TC-PTS Wind-Induced Vibration Response

In this section, the influence of different wind direction angles ( $\theta$  taken as  $0^\circ$ ,  $45^\circ$ ,  $60^\circ$ , and  $90^\circ$ ) on the maximum lateral displacement of the transmission line and the maximum tension of the supporting suspension cables of TC-PTS at  $V_{10} = 20\text{m/s}$  are investigated. The variation in the maximum lateral displacement of the transmission line and the maximum tension of the supporting suspension cable with the wind direction angle  $\theta$  is shown in Figure 9. In Figure 9a, it can be seen that the maximum lateral displacement of the transmission line increases with the increase in  $\theta$ , and initially it tends to be faster, and then slower, subsequently. In Figure 9b, the maximum tension of the supporting suspension cable increases with the increase in  $\theta$ . The change in the incremental magnitude of the maximum lateral displacement of the transmission line was also owing to the stress-stiffening effect of the structure. Considering the conductor as an example, the maximum lateral displacements of the conductor were 0.0071, 21.15, 28.12, and 32.96 m for wind direction angles of  $0^\circ$ ,  $45^\circ$ ,  $60^\circ$ , and  $90^\circ$ , respectively, and the most unfavorable wind direction angle for the maximum lateral displacement of the transmission line was  $90^\circ$ . The maximum tension of the supporting suspension cables increased with the wind direction angle because the downwind projected area of the transmission line was larger than that of the supporting suspension cables. As the wind direction angle increased, the global wind load on the structure increased. Therefore, the wind direction angle had a more significant effect on both the lateral displacement of the transmission line and the tension of the supporting suspension cables, and the most unfavorable wind direction angle for the two-span TC-PTS was  $90^\circ$ .

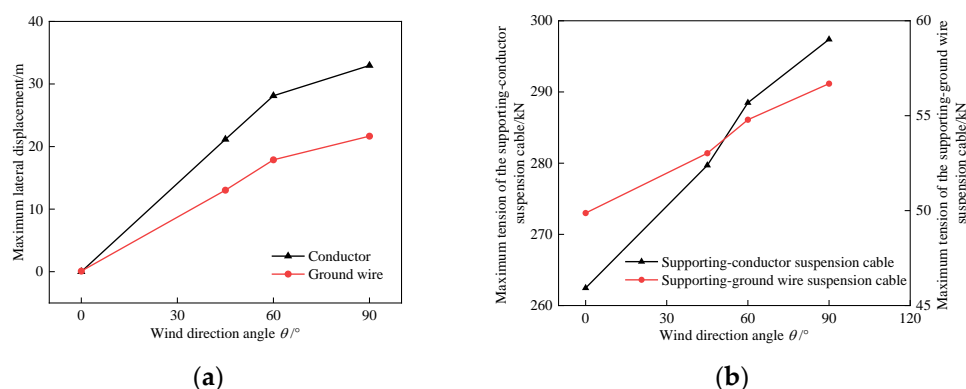


**Figure 9.** The influence of wind direction angle  $\theta$ . (a) Maximum lateral displacement of the transmission line; (b) maximum tension of the supporting suspension cable.

#### 4.2.3. Effect of Different Wind Speeds on the Wind-Induced Vibration Response of TC-PTS

Based on the conclusions of the above analysis, this section examines the effect of the change in wind speed  $V_{10}$  on the maximum lateral displacement of the transmission line and the maximum tension of the supporting suspension cables under the most unfavorable wind direction angle of  $90^\circ$  working conditions. The variation in the maximum lateral displacement of the transmission line and the maximum tension of the supporting suspension cable with the wind speed  $V_{10}$  at  $\theta = 90^\circ$  is shown in Figure 10. In Figure 10a, it can be

seen that the maximum lateral displacement of the transmission line increases with the increase in  $V_{10}$ , and the magnitude of the increase tends to be faster, initially, and becomes slow subsequently. This phenomenon is more obvious on the conductor. In Figure 10b, the maximum tension of the supporting suspension cables increases with the increase in  $V_{10}$  all the time. The change in the maximum lateral displacement increment of the transmission line is due to the stress stiffening effect of the structure. According to Equation (16), the element tangent stiffness increases with the increase in displacement, and the lateral stiffness of the structure also increases gradually with the increase in displacement. When the lateral stiffness is larger, the increase in lateral displacement of the transmission line will slow down.

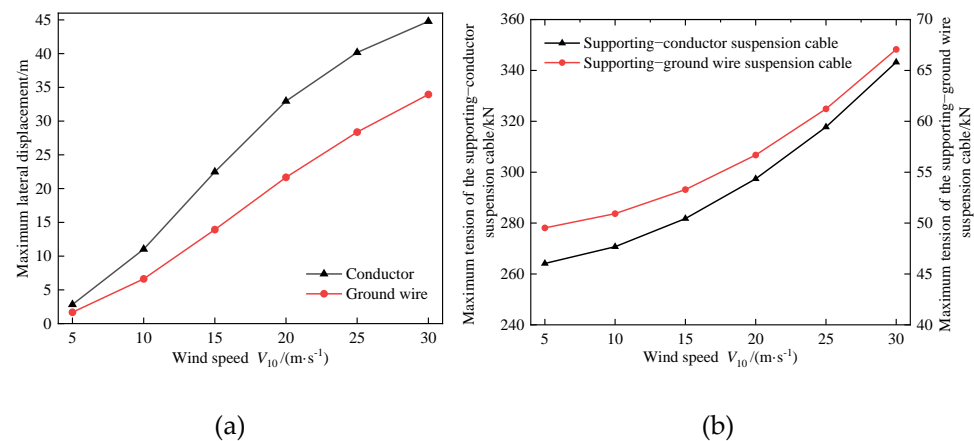


**Figure 10.** The influence of wind speed  $V_{10}$ . (a) Maximum lateral displacement of the transmission line; (b) maximum tension of the supporting suspension cable.

The maximum lateral displacement of a transmission line refers to the greatest horizontal movement experienced by the line due to external forces or factors. In this study, the maximum lateral displacement of the conductor is taken as a case in point. The wind speeds considered are 5, 10, 15, 20, 25, and 30 m/s, while the corresponding maximum lateral displacements of the conductor are measured as 2.83, 11.03, 22.48, 32.96, 40.16, and 44.78 m, respectively. The wind speed is from 5 m/s, and with every increase of 5 m/s, the maximum lateral displacement of the conductor increases by 8.20, 11.45, 10.48, 7.21, and 4.62 m, respectively. Therefore, in the case of smaller wind speed, the increase in wind speed will be higher. The maximum lateral displacement of the conductor increases by 8.20, 11.45, 10.48, 7.21, and 4.62 m. Therefore, the increase in wind speed increases the maximum lateral displacement of the transmission line more significantly when the wind speed is low, whereas the maximum lateral displacement of the transmission line is less affected by the wind speed when the wind speed is high. The change in the maximum tension of the supporting suspension cables is due to the fact that the suspension tension is required to balance the equivalent nodal loads, and the increase in wind speed increases the suspension tension all the time.

For the maximum tension of supporting suspension cables, taking the maximum tension of supporting-conductor suspension cable as an example, the wind speed starts from 5 m/s, and for every increase of 5 m/s, the maximum tension of the supporting-conductor suspension cable increases by 6.59, 11.05, 15.62, 20.38, and 25.47 kN, respectively, and the increment of the maximum tension is approximately linearly related to the wind speed, and the maximum tension and the quadratic of the wind speed are approximately linearly correlated. When the wind speed is small, the maximum tension of the supporting suspension cable is less affected by wind speed, while when the wind speed is larger, the maximum tension of the supporting suspension cable is more significantly affected by wind speed.

Therefore, at lower wind speeds  $V_{10}$ , the lateral displacement of the transmission line was more affected by the wind speed than the tension of the supporting suspension cable, and at higher wind speeds  $V_{10}$ , the tension of the supporting suspension cable was more notably affected by wind speeds than the lateral displacement of the transmission line.

#### 4.3. Wind-Induced Fatigue Damage of TC-PTS

##### 4.3.1. Wind-Induced Fatigue Damage Assessment of TC-PTS

To comprehensively analyze the wind vibration fatigue damage condition of the two-span TC-PTS, the ends and midpoint of the supporting-conductor suspension cable and conductor were selected as fatigue analysis parts. The ends and midpoint of the supporting-conductor suspension cable and conductor are points A, B, C, and D, respectively. The wind-induced fatigue damage of each fatigue analysis part of the two-span TC-PTS was calculated by considering the working conditions of wind speed  $V_{10} = 15\text{m/s}$  and wind direction angle  $\theta = 90^\circ$  as examples. The stress time history of each fatigue analysis part is shown in Figure 11, and the corresponding mean stress, mean square deviation, and fatigue damage are listed in Table 4. It can be observed that, compared with point A, the stress mean value of point B is larger, but the mean square deviation is smaller, and its fatigue damage is smaller because the stress amplitude has a more significant effect on the fatigue damage value: the larger the mean square deviation, the more frequently the high stress amplitude occurs, and the more serious the corresponding fatigue damage. The mean stress value and mean square deviation of point C were greater than those of point D, and the fatigue damage value was also greater.

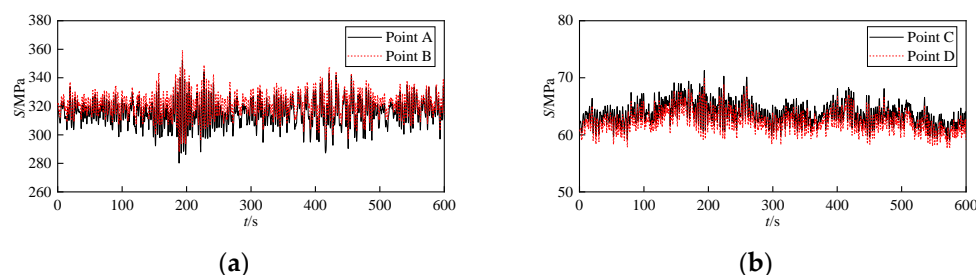


**Figure 11.** Stress time history of each part. (a) The supporting-conductor suspension cable; (b) the conductor.

**Table 4.** Fatigue damage of each part.

Part	Mean Value of Stress/(MPa)	Mean Square Deviation of Stress/(MPa)	Fatigue Damage
Point A	315.04	9.12	$9.70 \times 10^{-11}$
Point B	320.96	8.37	$7.79 \times 10^{-11}$
Point C	63.70	1.87	$1.41 \times 10^{-12}$
Point D	62.36	1.83	$4.96 \times 10^{-13}$

##### 4.3.2. Effect of Different Wind Direction Angles on Wind-Induced Fatigue Damage of TC-PTS

At  $V_{10} = 20\text{ m/s}$ , the influences of different wind direction angles  $\theta$  on the fatigue damage of various parts of the TC-PTS are listed in Table 5. With a gradual increase in the wind direction angle, the wind load acting on the conductor is larger because of the coupling effect between the conductor and the supporting-conductor suspension cable, and the load borne by the supporting-conductor suspension cable also gradually increases. Therefore, the fatigue damage of each part increases. In the same working conditions, the fatigue damage of the supporting-conductor suspension cable end (point A) is larger than that of the midpoint (point B), while the fatigue damage of the conductor end (point C) is smaller than that of the midpoint (point D). It is easy to see that, among all the

wind direction angles, the  $90^\circ$  wind direction angle has the most significant effect on the wind-induced fatigue damage of the TC-PTS.

**Table 5.** Fatigue damage of each part under different wind directions.

Case	Wind Direction/( $^\circ$ )			
	0	45	60	90
Point A	$2.91 \times 10^{-12}$	$4.43 \times 10^{-11}$	$2.72 \times 10^{-10}$	$1.80 \times 10^{-9}$
Point B	$3.30 \times 10^{-12}$	$1.29 \times 10^{-11}$	$1.43 \times 10^{-10}$	$8.87 \times 10^{-10}$
Point C	$2.01 \times 10^{-14}$	$1.17 \times 10^{-13}$	$1.33 \times 10^{-12}$	$6.13 \times 10^{-11}$
Point D	$1.50 \times 10^{-14}$	$5.25 \times 10^{-13}$	$9.28 \times 10^{-12}$	$4.11 \times 10^{-10}$

#### 4.3.3. Effect of Different Wind Speeds on Wind-Induced Fatigue Damage of TC-PTS

Under the  $90^\circ$  wind direction angle condition, the effect of wind speed  $V_{10}$  change on the fatigue damage of each part of TC-PTS is shown in Table 6. As shown in the table, the wind-induced fatigue damage of each part increases with an increase in the wind speed  $V_{10}$ , and the fatigue damage at the end of the supporting-conductor suspension cable (point A) is larger than the fatigue damage of the midpoint (point B) under the same working conditions. With the gradual increase in wind speed  $V_{10}$ , the fatigue damage to all parts of the supporting-conductor suspension cable and conductor showed a tendency to increase faster and then slower. The fatigue damage of all parts of the supporting-conductor suspension cable increased gradually from  $10^{-16}$  to  $10^{-8}$ , whereas the fatigue damage of all parts of the conductor increased gradually from  $10^{-25}$  to  $10^{-7}$ . When the wind direction angle was  $90^\circ$ , the wind load per unit length of the conductor was greater than that of the supporting-conductor suspension cable, and the fatigue damage of each part of the conductor increased more than that of the supporting-conductor suspension cable.

**Table 6.** Fatigue damage of each part under different wind speeds.

Wind Speed/( $m \cdot s^{-1}$ )	Point A	Point B	Point C	Point D
5	$1.40 \times 10^{-15}$	$1.31 \times 10^{-16}$	$1.14 \times 10^{-24}$	$2.64 \times 10^{-25}$
10	$2.87 \times 10^{-12}$	$1.59 \times 10^{-13}$	$5.13 \times 10^{-18}$	$1.47 \times 10^{-16}$
15	$9.70 \times 10^{-11}$	$7.79 \times 10^{-11}$	$1.41 \times 10^{-12}$	$4.96 \times 10^{-13}$
20	$1.80 \times 10^{-9}$	$8.87 \times 10^{-10}$	$6.13 \times 10^{-11}$	$4.11 \times 10^{-10}$
25	$7.72 \times 10^{-9}$	$3.84 \times 10^{-9}$	$1.59 \times 10^{-8}$	$8.39 \times 10^{-8}$
30	$5.81 \times 10^{-8}$	$1.70 \times 10^{-8}$	$8.03 \times 10^{-7}$	$3.32 \times 10^{-7}$

## 5. Conclusions

The TC-PTS is a new class of power transmission structures suitable for mountainous terrain. A nonlinear finite element model of the wind-induced vibration of the TC-PTS was proposed using the nonlinear finite element method. Wind-induced vibration response analysis and fatigue damage assessment were performed for a two-span TC-PTS, and the effects of wind speed and wind direction angle on the wind-induced vibration response and fatigue damage of the TC-PTS were discussed. The main conclusions are as follows:

- (1) The proposed model calculates the natural frequency and displacement time history with high accuracy and efficiency, and the computational cost of obtaining the dynamic response is only 4.19% of that of ANSYS.
- (2) For the mean wind load, at smaller wind speeds, the lateral displacement of the transmission line is more affected by wind speeds than the tension of the supporting suspension cable; at larger wind speeds, the tension of the supporting suspension cable is more notably affected by wind speeds than the lateral displacement of the transmission line.
- (3) The fatigue damage value at the end of the supporting-conductor suspension cable was slightly greater than that at the midpoint. For the conductor, under the wind

direction angle cases, the midpoint fatigue damage value is greater than the end fatigue damage value, whereas under the wind speed cases, the end and midpoint fatigue damage values have no obvious comparison.

- (4) The wind-induced vibration response and fatigue damage of TC-PTS were significantly affected by the wind direction angle, and the results of the arithmetic analysis showed that the most unfavorable wind direction angle for TC-PTS was  $90^\circ$ .

Although this paper proposes a framework for the wind-induced vibration response analysis and fatigue damage assessment of TC-PTS, there still remain aspects that can be improved further. For example, the design wind speed or extreme wind speed characteristics of the terrain where TC-PTS is located may differ from the characteristics of the flat ground wind field. The design wind speed or extreme wind speed of the terrain where TC-PTS is located can be obtained by field measurement or other methods, and then the impact of its uncertainty on the wind-induced vibration response and fatigue damage of TC-PTS can be considered.

**Author Contributions:** Conceptualization, Z.L. and T.W.; methodology, T.W.; software, J.L. and B.W.; validation, Z.L., T.W., and J.L.; formal analysis, T.W.; investigation, T.W., B.W., and J.L.; resources, Z.L.; data curation, B.W.; writing—original draft preparation, J.L.; writing—review and editing, J.L. and B.W.; visualization, B.W.; supervision, T.W.; project administration, T.W.; funding acquisition, T.W. All authors have read and agreed to the published version of the manuscript.

**Funding:** The research presented in this paper was supported by the Special Support of Chongqing Postdoctoral Research Project (the funding number 2022CQBShBT3009) and the Special Postdoctoral Support Project of Chongqing Research Institute of HIT (the funding number KY506023002).

**Data Availability Statement:** The data presented in this study are available on request from the corresponding author. The data are not publicly available due to the ongoing research work.

**Conflicts of Interest:** The authors declare no conflict of interest.

## References

1. Bai, H.; Yi, T.; Li, H.; Ren, L. Multisensors on-site monitoring and characteristic analysis of UHV transmission tower. *Int. J. Distrib. Sens. Netw.* **2012**, *8*, 545148. [\[CrossRef\]](#)
2. Lou, W.; Wu, D.; Liu, M.; Zhang, L.; Bian, R. Properties of mountainous terrain wind field and their influence on wind-induced swing of transmission lines. *China Civ. Eng. J.* **2018**, *51*, 46–55+77.
3. Irvine, H. *Cable Structure*; The MIT Press: New York, NY, USA, 1981.
4. McClure, G.; Lapointe, M. Modeling the structural dynamic response of overhead transmission lines. *Comput. Struct.* **2003**, *81*, 825–834. [\[CrossRef\]](#)
5. Kempner, L.; Smith, S. Cross-rope transmission tower-line dynamic analysis. *J. Struct. Eng. ASCE* **1984**, *110*, 1321–1335. [\[CrossRef\]](#)
6. Tian, L.; Pan, H.; Ma, R.; Dong, X. Seismic failure analysis and safety assessment of an extremely long-span transmission tower-line. *Struct. Eng. Mech.* **2019**, *71*, 305–315.
7. Fu, X.; Li, H.; Tian, L.; Wang, J.; Cheng, H. Fragility analysis of a transmission line subjected to wind loading. *J. Perform. Constr. Facil. ASCE* **2019**, *33*, 04019044. [\[CrossRef\]](#)
8. Yan, Z.; Savory, E.; Li, Z.; Lin, W. Galloping of iced quad-conductors bundles based on curved beam theory. *J. Sound Vib.* **2014**, *333*, 1657–1670. [\[CrossRef\]](#)
9. Yan, Z.; Li, Z.; Savory, E.; Lin, W. Galloping of a single iced conductor based on curved-beam theory. *J. Wind Eng. Ind. Aerodyn.* **2013**, *123*, 77–87. [\[CrossRef\]](#)
10. Chunming, W.; Bin, M.; Tingting, S. Research on the wind-induced vibration coefficient of transmission tower-line system. *Phys. Procedia* **2012**, *24*, 149–154. [\[CrossRef\]](#)
11. Saffari, P.R.; Sirimontree, S.; Thongchom, C.; Thira, J.; Pouyan, R.S.; Suraparb, K.; Suphanut, K. Free and forced vibration of sandwich fgm porous variable thickness nanoplates integrated with magneto-electro-elastic layers via nonlocal strain gradient theory. *Eng. Sci.* **2023**, *24*, 918. [\[CrossRef\]](#)
12. Huang, H.; Xian, Y.; Zhang, W.; Guo, M.; Yang, K.; Xi, K. Analysis of wind-induced vibration of a spoke-wise cable-membrane structure. *J. Mar. Sci. Eng.* **2020**, *8*, 603. [\[CrossRef\]](#)
13. Liu, X.; Yan, B.; Zhang, H.; Zhou, S. Nonlinear numerical simulation method for galloping of iced conductor. *Appl. Math. Mech.* **2009**, *30*, 489–501. [\[CrossRef\]](#)
14. Rong, X.; Xie, A.; Zhao, P.; Yang, M.; Bu, J.; Wei, X. Fatigue performance of composite trough-girders with corrugated-steel-webs. *J. Constr. Steel Res.* **2023**, *207*, 107974. [\[CrossRef\]](#)

15. Wang, S. *Damage Detection and Evaluation of Stud Connector of Composite Girder Bridge Based on Acoustic Emission Technology*; Shijiazhuang Tiedao University: Shijiazhuang, China, 2023.
16. Yan, Z.; Huang, J.; Li, Z. Finite element model of bundle lines based on 6-dof node. *Eng. Mech.* **2012**, *29*, 325–332.
17. Zhu, Z.; Meguid, S. Analysis of three-dimensional locking-free curved beam element. *Int. J. Comput. Eng. Sci.* **2004**, *5*, 535–556. [[CrossRef](#)]
18. Zhu, Z.; Meguid, S. Vibration analysis of a new curved beam element. *J. Sound Vib.* **2008**, *309*, 86–95. [[CrossRef](#)]
19. Chen, Z.; Zeng, Q.; Yan, Q. A UL formulation for internal force analysis of spatial frame structures with large displacement. *China Civ. Eng. J.* **1992**, *25*, 34–43.
20. Shi, H.; Salim, H. Geometric nonlinear static and dynamic analysis of guyed towers using fully nonlinear element formulations. *Eng. Struct.* **2015**, *99*, 492–501. [[CrossRef](#)]
21. Liu, S. Accurate analysis method on the tangential stiffness matrix of pinned straight rod element. *Chin. J. Comput. Mech.* **2014**, *31*, 48–53.
22. Desai, Y.; Yu, P.; Popplewell, N.; Shah, A. Finite element modelling of transmission line galloping. *Comput. Struct.* **1995**, *57*, 407–420. [[CrossRef](#)]
23. Jakob, M. Wind field simulation. *Probabilistic Eng. Mech.* **1998**, *13*, 269–282.
24. *GB 50009-2012*; Load Code for the Design of Building Structures. China Architecture & Building Press: Beijing, China, 2012.
25. Wang, X. *Finite Element Method*; Tsinghua University Press: Beijing, China, 2003.
26. Yan, L.; Li, J.; He, X. Effect of central clamps on fatigue damage of suspenders of suspension bridge under joint action of fluctuating wind and vehicle loads. *J. Cent. South Univ.* **2023**, *54*, 1393–1406. [[CrossRef](#)]
27. Kong, D.; Li, L.; Long, X.; Ye, Z. Parametric investigation on fatigue life of transmission line subjected to Aeolian vibration. *J. Wuhan Univ. Technol.* **2010**, *32*, 53–57.

**Disclaimer/Publisher's Note:** The statements, opinions and data contained in all publications are solely those of the individual author(s) and contributor(s) and not of MDPI and/or the editor(s). MDPI and/or the editor(s) disclaim responsibility for any injury to people or property resulting from any ideas, methods, instructions or products referred to in the content.